ChemSusChem

Research Article
doi.org/10.1002/cssc.202401304

Chemistry Europe
European Chemical Societies Publishing

www.chemsuschem.org

Boron Surface Treatment of $Li_7La_3Zr_2O_{12}$ Enabling Solid Composite Electrolytes for Li-Metal Battery Applications

Ignacio Cuevas,[a] Kenza Elbouazzaoui,[a] Mario Valvo,[a] Jonas Mindemark,[a] Daniel Brandell,*[a] and Kristina Edström[a]

Despite being promoted as a superior Li-ion conductor, lithium lanthanum zirconium oxide (LLZO) still suffers from a number of shortcomings when employed as an active ceramic filler in composite polymer–ceramic solid electrolytes for rechargeable all-solid-state lithium metal batteries. One of the main limitations is the detrimental presence of Li_2CO_3 on the surface of LLZO particles, restricting Li-ion transport at the polymer–ceramic interfaces. In this work, a facile way to improve this interface is presented, by purposely engineering the LLZO particle surfaces for a better compatibility with a PEO:LiTFSI solid polymer electrolyte matrix. It is shown that a surface treatment based on immersing LLZO particles in a boric acid solution can improve the LLZO surface chemistry, resulting in an enhancement in the ionic conductivity and cation transference number of the CPE with 20 wt% of boron-treated LLZO particles compared to the analogous CPE with non-treated LLZO. Ultimately, an improved cycling performance and stability in Li//$LiFePO_4$ cells was also demonstrated for the modified material.

Introduction

Due to their high energy density, lithium-ion batteries dominate the portable energy storage landscape.[1] However, as batteries get bigger in size, associated with the widespread use of full electric vehicles, their safety issues become more prominent.[2–4] Problems related to leakage, flammability and toxicity of ubiquitous organic liquid electrolytes in Li-ion batteries have pushed the research in this field to focus also on safety-enhancing additives, alternative liquid electrolyte formulations and solid electrolytes.[5–7] Most importantly, solid electrolytes potentially enable higher energy densities compared to conventional Li-ion batteries through the use of Li metal anodes.[8]

Research on solid electrolytes has significantly progressed in the latest years, yet a number of major challenges still needs to be fully addressed to enable their possible large-scale fabrication and implementation.[8,9] For example, solid polymer electrolytes (SPEs) constitute a promising class of solid electrolytes thanks to their flexibility and good interfacial properties. However, poor ionic conductivity at room temperature remains a fundamental shortcoming of SPEs. In contrast, much higher values of ionic conductivity can be provided by inorganic solid electrolytes (ISEs). However, ISEs often present a number of other problems, such as a possible narrow electrochemical window and poor interfacial contacts with the electrodes, let alone their inherent stiffness. Hence, the assembly of battery cells with ISEs is often a highly critical aspect, limiting their market potential and consequently pushing towards novel approaches in this direction. One route forward could be employing solid composite polymer electrolytes (CPEs).[10] CPEs have been widely investigated with poly(ethylene oxide) (PEO) as a benchmark polymer matrix. Depending on the design of CPEs, an increase in PEO's amorphicity and thereafter a higher ionic conductivity could be achieved.[11–13]

Such composite electrolytes can potentially benefit from the characteristics of easy processability and good interfacial contact of polymers, combined with the high ionic conductivity arising from Li-ion-conductive ceramic materials.[14–17] Garnet-type $Li_7La_3Zr_2O_{12}$ (LLZO) has been widely employed as an active ceramic filler in CPEs, to profit from its high Li-ion conductivity (up to ~1 mS cm^{-1} at room temperature) and alleged chemical inertness that should sustain a wide electrochemical stability window (ESW) of ~0–6 V *vs.* Li^+/Li. Given the high Li-ion conductivity of LLZO, most studies on CPEs focused on incorporating LLZO ceramic filler into a polymer matrix to maximize the CPEs ionic conductivity through an access to the bulk LLZO as a Li^+ transport pathway. To this end, it has been shown that the ionic transport in LLZO-based CPEs can be influenced by the ceramic loadings.[18] In fact, LLZO could act as an additional source of Li^+, thereby ideally increasing the ionic conductivity of the CPEs to values approximately comparable to those of LLZO itself when increasing the ceramic content. However, this has not been practically achieved yet, and on the contrary, lower conductivities at higher ceramic loadings have generally been observed.[19,20] This could suggest that there is a trade-off between different competing effects determining the ionic conduction trend in LLZO-based CPEs. While the ceramic loading is surely one factor among many, it was revealed that

[a] *Department of Chemistry – Ångström Laboratory, Uppsala University, Uppsala, Sweden*

***Correspondence:** Daniel Brandell, Department of Chemistry – Ångström Laboratory, Uppsala University, Box 538, SE-751 21 Uppsala, Sweden.*
Email: Daniel.Brandell@kemi.uu.se

Supporting Information for this article is available on the WWW under https://doi.org/10.1002/cssc.202401304

the ionic transport could also be influenced by the accessible transport pathways in the CPE system. In this context, it has been shown that upon incorporating LLZO particles, an additional transport pathway along polymer–ceramic interfaces can be formed and Li^+ transport could preferentially happen at that interface, contributing to enhance the ionic conductivity of CPEs.[21] However, when correlating the ceramic loadings to interfacial transport pathways, one would expect higher ionic conductivity for higher ceramic loadings. In contrast, that is not what is generally observed, and it becomes unclear what parameters govern the Li^+ transport, suggesting that additional factors could play a key role in the Li^+ transport in LLZO-based CPEs. To this end, it was suggested that the ionic conduction mechanism could also be dependent on interactions between the ions from the polymer matrix and the surface of the ceramic particles, leading to a weaker polymer–cation coordination or reduced ion pairing in the CPE system. Connecting the dots, it becomes clear that LLZO surface chemistry plays a key role in the aforementioned contributions and governs the Li^+ transport in LLZO-based CPEs.[22,23]

Li_2CO_3 spontaneously forms on the surface of LLZO particles during synthesis due to air exposure, hindering its performance by rendering the Li-ion transport pathway along the polymer–ceramic interfaces unfavourable, and limiting interactions between different components.[24–27] An often neglected, yet crucial, aspect of such Li_2CO_3 formation on the LLZO surface is its surface affinity towards other species. It is well-known that the LLZO surface affinity for lithium substantially improves if the lithium carbonate layer is addressed.[28,29] The weak adhesion to Li_2CO_3-contaminated LLZO surfaces arises from a rather inert surface composition, which negatively impacts its contact properties with other solids. Therefore, it is expected that the successful incorporation of active LLZO particles in the polymer matrix will directly depend on the mutual surface chemistry, and hence engineering the contact between the polymer and the ceramic phases through eliminating or converting such Li_2CO_3 layer is crucial to optimize the ultimate ionic conductivity of CPEs. Accordingly, this approach revolving around a purposely-modified LLZO surface has emerged as a primary focus for developing LLZO-based CPEs.[30–32]

In this study, we aim to explore the effect of modifying the LLZO surface on the corresponding CPE properties. To this end, we investigate a 'ceramic-in-polymer' composite electrolyte system, utilizing a PEO:LiTFSI polymer matrix together with LLZO as an active ceramic filler and employing a similar approach as those previously reported for surface modifications of pelletised LLZO.[18,20–22] Surface modification of LLZO powders would inherently imply different considerations when compared to its pellet counterpart (e.g. larger surface areas, intimate mix between solid and liquid), nevertheless its interest in the ISEs field is unquestionable.[36] Fine-grained LLZO powders are submerged in boric acid solution in ethanol, which constitutes a straightforward way to form a functional $LiBO_2$ layer on their surface.[29] Both non-treated and boron-treated LLZO particles are thereafter incorporated in the PEO:LiTFSI matrix, highlighting the impact of the LLZO surface modification on the structure, morphology, ionic conductivity and electrochemical properties of the corresponding CPEs. As it will be shown, although such chemical changes at the LLZO/PEO:LiTFSI interface can appear minor, their impact on the resulting properties of the CPE are indeed significant.

Results and Discussion

As-synthesized LLZO powders were characterized before and after their surface modification by means of XRD to ensure that no significant decomposition of the highly ion-conductive cubic phase or formation of new crystalline phases occurred during and/or after the treatment. The diffraction patterns in Figure 1a show two virtually identical results for both the boron-treated LLZO powders and their non-modified counterparts. Despite the measurement being carried out in atmospheric conditions, the quick transfer from the Argon-filled glovebox and the immediate XRD measurement thereafter allowed for almost negligible crystalline Li_2CO_3 formation on the LLZO particle surfaces. The Li_2CO_3 impurity, often displayed as a rather visible characteristic peak at around 23° can barely be seen here, while all the diffraction peaks corresponding to the LLZO cubic phase are clearly present and well defined.[37] Therefore, the treatment does not seem to trigger any structural change in the LLZO powders and the crystal structure of the cubic phase with its Ia-3d space group is clearly retained. However, the treatment appears to cause other changes to the material, as the treated LLZO powders display a greater tendency to form aggregates during handling.

Due to the differences observed when handling the powders (grinding, sieving, and transferring to containers until later use - in all cases showing a greater tendency for aggregation when the powders were treated), further investigations were carried out to better understand the morphology, composition and chemical features of the grain surfaces. SEM imaging of the respective powders reveals a significant difference between the two samples. While the grain sizes after high-energy ball milling and subsequent sieving should be similar, the tendency of the treated powders to agglomerate is obvious. Large agglomerates are visible in both Figure 1b&c, which correspond to the boron-treated powders. At lower magnifications (1000×, Figure 1b) a rather granular texture appears, which clearly contrasts with the texture shown in Figure 1d, where the non-treated powders display a more homogenous distribution in which the boundaries among the grains can barely be observed. At higher magnifications (5000×), Figure 1c&e reveal several relevant features. The grains are irregularly shaped in both sets of samples, with a presence of larger grains (likely a result of agglomeration of individual grains) up to ten microns in width and small grains that appear to be well below micron-sized dimensions.

Due to the irregularity of grain sizes and shapes, for which rather large agglomerates are observed (which may or may not break upon milling and mixing with the polymer to form composites); it is difficult to assess the final size of the grains ultimately introduced into the composites. Nevertheless, DLS measurements should give a realistic insight into the maximum

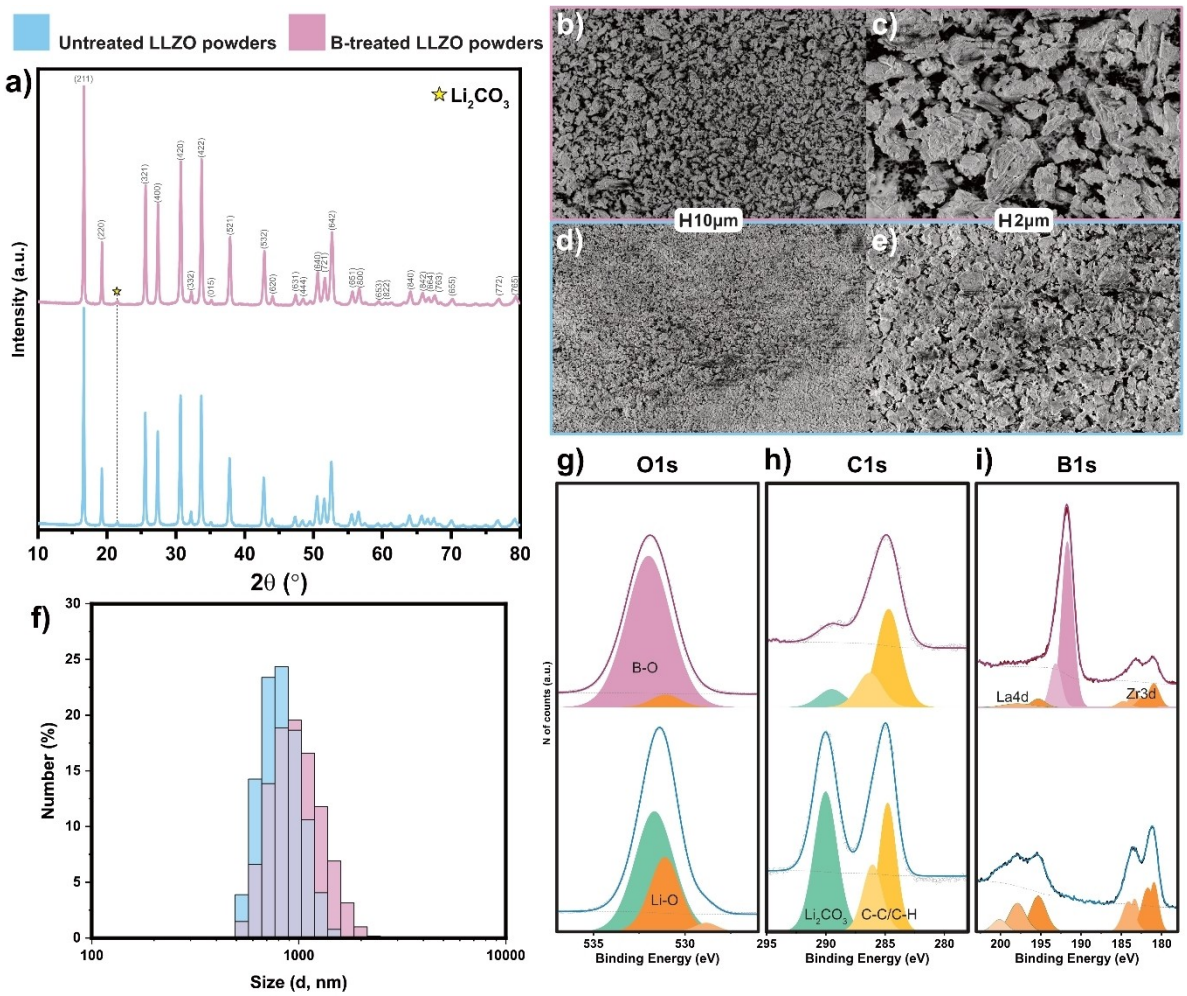

Figure 1. Characterisations of the synthesized LLZO powders. (a) XRD patterns for treated (top) and untreated (bottom) LLZO powders, with related Miller indexes of the main diffraction peaks in grey, and a slight – yet observable – contribution of Li_2CO_3 indicated by a yellow star. SEM images of (b&c) treated and (d&e) non-treated LLZO powders originally recorded at 1000× magnification (b&d) and 5000× magnification (c&e), respectively. (f) Particle size distributions by percentage for both boron-treated (pink) and non-treated (light blue) LLZO powders obtained via DLS measurements. Note in (f) that the light violet part of the histogram corresponds to the overlap between both curves, and illustrates that, despite a higher number of bigger grains for the boron treated samples, both distributions are rather similar. (g, h&i) XPS spectra of treated (top row) and untreated (bottom row) LLZO powders for their characteristic O1s, C1s and B1s regions. Note the striking difference in the B1s region, indicating the formation of boron-rich surface compounds that coexist with an almost complete neutralisation of the Li_2CO_3 peak for the treated powders.

size of the agglomerates, which are most likely milled during the composite preparation. Figure 1a shows the particle size distributions for both the treated and non-treated LLZO powders. In accordance with the SEM results, the findings from the DLS analysis highlight a higher degree of polydispersity and a higher mean grain diameter for the treated powders, as summarized in Table 1. The average grain size in both cases, as extracted from the DLS data, is around 1 μm, yet the distinctive tendency for flocculation for the treated powders leads to a higher observed particle size, both in the final DLS results from Table 1 and from the SEM results in Figure 1. Additional details on the DLS results, as well as the autocorrelation function, can be found separately in Figure S1, which also includes the distribution plots associated with the Zeta potential measurements. The results of the Zeta (ζ) potential values show that, despite both sets of powders being handled similarly, both the electrophoretic mobility and Zeta potential distributions were broader and their maxima were shifted to higher positive values for the non-treated powders, when compared with those of the boron-treated powders. This is illustrative of the difference in surface chemistry between the two sets of powders, which might be a consequence of the difference in pH. Despite identical handling of the samples, the resulting pH is slightly more acidic (pH~6) for the boron-treated powders than for the non-treated powders (pH~7). The implications of this deviation

Table 1. Average grain size and ζ-potential for boron-treated LLZO powders (BT-LLZO; light pink) and non-treated LLZO powders (NT-LLZO; light blue).

Sample	Z-average d (nm)	St. Dev. d (nm)	ζ-potential (mV)	St. Dev. (mV)
BT-LLZO	1157	300	−2.12	42.6
NT-LLZO	875.6	177	10.1	54

might justify the substantial shift of the ζ-potential values from 10.1 mV for the non-treated powders to −2.12 mV for the treated powders. The differences for the ζ-potential and the pH might have several concurrent effects on the CPEs. The change of sign for the ζ-potential implies a mostly negatively charged surface of the treated LLZO particles, which would in principle be more easily attracted to positively charged species from the polymer matrix, such as lithium ions. These charged species could be either cations coordinated to ether groups from the polymer backbone, or Li^+ cations forming ion pairs or clusters together with $TFSI^-$ anions.

Enhancing the ionic transport properties of CPEs could be achieved differently, either by a possible particle–ion interaction or by reduction of the polymer crystallinity, which can provide more amorphous regions where the ionic transport usually occurs, and in a concurrent creation of additional ion transport pathways along the polymer–ceramic interfaces.[38–40] Other suggestions for an increased ionic conductivity upon addition of ceramic particles include transportation through the ceramic bulk phase, as well as chemical interactions between the polymeric and ceramic phases which indirectly shift the distribution of salt coordination structures.[41] This latter phenomenon would occur due to Lewis acid–base interactions which generate immobilized anions on the surface of the ceramic particles, which in turn lead to a weakening of the bond between Li^+ and $TFSI^-$, and thereby a reduced amount of ion pairs and more free charge carriers in the CPE.[17,42–44] Although the ζ-potential value is most likely different in the suspension with isopropyl alcohol as compared to the PEO:LiTFSI system, the ζ-potential figure will likely remain more negative for the treated particles with respect to that of their untreated counterpart, thereby causing a possible accumulation of Li^+ on the surface of the ceramic phase after the H_3BO_3 treatment. Additionally, the low absolute value of the ζ-potential for the treated powders might explain the observation of increased flocculation. As the neat charges on the ceramic surface are less intense, the repelling forces among the LLZO particles are reduced, thus leading to the formation of clusters in solution.

To further explore the characteristics of the ceramic surfaces, XPS measurements were carried out for both treated and non-treated powders, as presented in Figure 1g–i. The presence of a mostly boron-based layer on the outermost surface of the particles is observed for the treated LLZO powders. The peak just below 192 eV in the B1s region in Figure 1i corresponds well with previously reported values for $LiBO_2$, and clearly differs from the typical 193 eV position for H_3BO_3,[45] which is used in the former treatment of the LLZO powders. The presence of lithium in both samples (Figure S2) indicates that the acid treatment generates additional species that are not merely H_3BO_3 deposits on the LLZO surface and that the newly formed surface compounds containing boron and oxygen also include lithium. This could be $LiBO_2$ forming a surface layer preventing Li_2CO_3 formation, and favouring not only the ionic transport along the polymer-ceramic interfaces, but also any possible ceramic-salt interaction.[46–48] The $LiBO_2$ formation is likely associated with a concomitant neutralisation via removal, transformation or shielding of the detrimental Li_2CO_3 layer on the LLZO surface, which severely hinders Li-ion conduction. As it can be seen in Figure 1h, the carbonate peak (190 eV) is largely suppressed in the C1s spectra of the LLZO powders treated with H_3BO_3. The presence of bulk contributions in the treated powders (highlighted in orange in both the O1s and B1s regions) certainly indicates that the Li_2CO_3 is not buried underneath a thicker boron-based layer, but rather disappears almost completely as a result of the H_3BO_3 treatment. As an additional insight, the O1s spectra clearly indicates that the formed $LiBO_2$ layer is thicker and more homogenous than the carbonate layer, yet with metal-oxygen contributions from the bulk still distinguishable and thus falling within the probing range of XPS.

To elucidate the effect of the surface treatment of LLZO, both non-treated and treated LLZO particles were incorporated as ceramic fillers to fabricate CPEs based on a PEO:LiTFSI polymer matrix. The obtained free-standing films were first subjected to structural characterization. Figure 2a displays the XRD patterns of the filler-free SPE, as well as the composite electrolytes with 20 wt% of non-treated and boron-treated LLZO particles, labelled CPE20NT and CPE20BT, respectively. PEO is a semi-crystalline polymer and shows two characteristics diffraction peaks around 20° and 24°, which are clearly retained after the addition of LLZO particles. Furthermore, all characteristic peaks of the cubic LLZO phase can be clearly observed for both CPE20NT and CPE20BT, and no striking changes or additional peaks are seen. This indicates that the resulting CPEs are structurally stable upon adding LLZO ceramic filler and no formation of new crystalline phases occurs for the LLZO compound itself. Additionally, the polymer matrix coordination chemistry should also remain stable after incorporating the LLZO ceramic filler. In Figure 2c all characteristic vibrations of PEO are observed in the corresponding FTIR spectra for both SPE and CPEs with 20 wt% of non-treated and boron-treated LLZO particles, respectively. A similar finding is observed for higher ceramic loadings, up to 40 wt%, as displayed in Figure S6. This indicates that the polymer–lithium salt coordination remains unchanged and no polymer degradation occurs after LLZO is being added to form a CPE system.

Figure 2d–f shows the SEM images of the surface morphology of the CPE with boron-treated LLZO, CPE with non-treated LLZO and the filler-free SPE, respectively. As it can be seen from the similarity of these three micrographs, most of the imaged surface corresponds to the polymer matrix. The surface of the CPE with boron-treated LLZO seems to be slightly more homogeneous than that of the CPE with unmodified particles. In order to provide further insights on the morphology of the composite samples, the films were cut inside an argon-filled glovebox and mounted onto a cross-section sample holder to record SEM micrographs (Figure 2g and h). In both cases, despite the difference of the angle under which the samples are observed, it clearly appears that multiple LLZO grains are present throughout the otherwise homogeneous, smooth layer. The roughness due to the presence of the ceramic grains is more apparent for the CPE with non-treated LLZO (Figure 2h). This might be explained through a less integrated incorporation

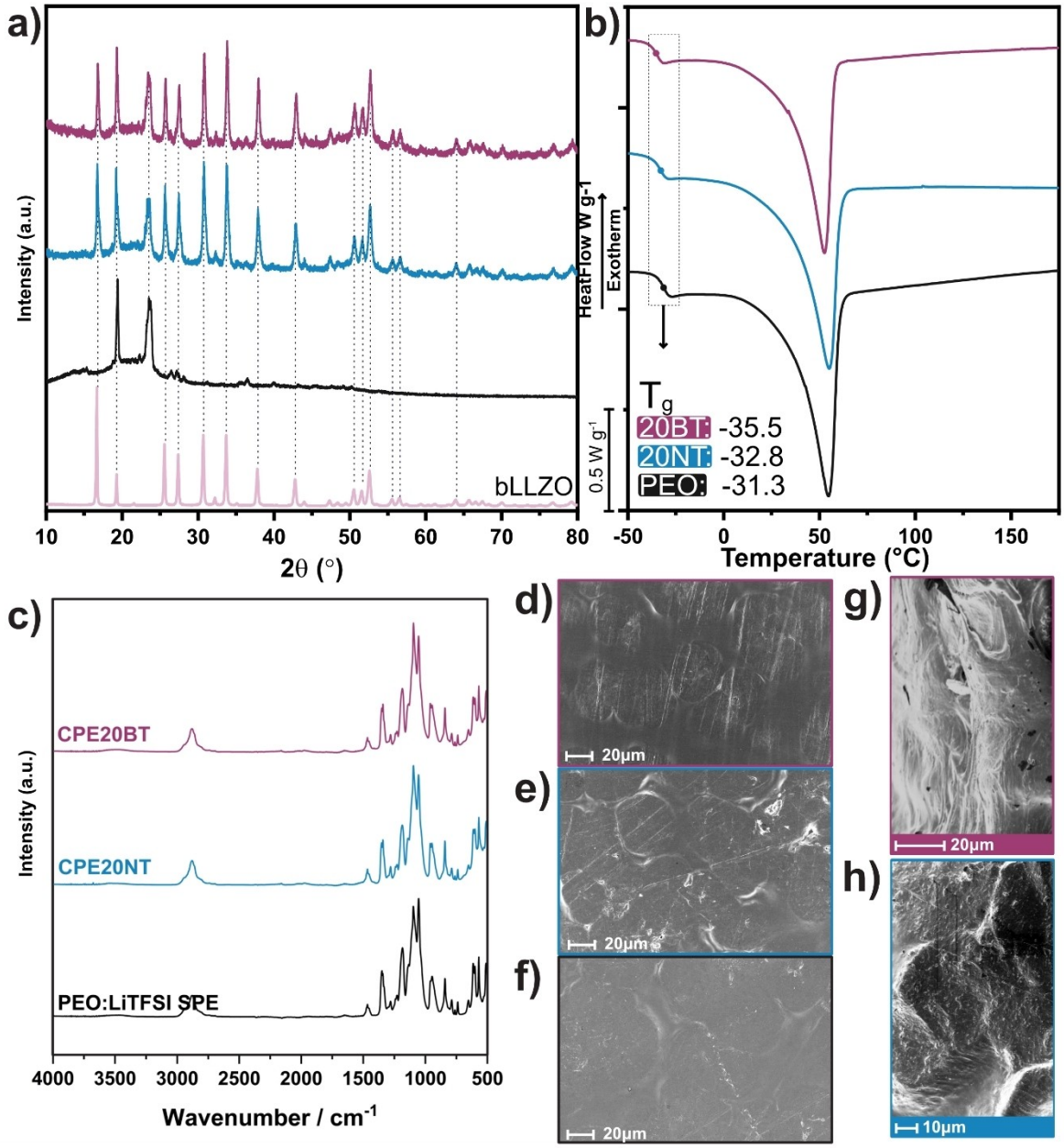

Figure 2. Characterisation of SPE, CPEs and LLZO powders. (a) XRD patterns for CPE containing boron-treated LLZO (top, magenta), CPE with non-treated LLZO (second from top, dark blue), SPE (third from top, black) and boron-treated LLZO powder (bottom, pink) as a reference for the LLZO characteristic peak positions. (b) DSC curves for the SPE and CPEs, with a legend indicating the value of the inflection point to determine the glass transition temperature, T_g. (c) FTIR spectra of SPE, CPE20NT and CPE20BT at room temperature. SEM images providing an in-plane view at 1000× magnification of the respective surfaces of (d) boron-treated LLZO:CPE, (e) non-treated LLZO:CPE, and (f)SPE. Cross-section SEM images at 1000× magnification for (g) boron-treated LLZO:CPE and (h) non-treated LLZO:CPE, respectively. Note that the scale bar in g) is 20 μm, while in h) is 10 μm.

of the LLZO particles in the polymer matrix, which could be due to a lack of chemical compatibility with the SPE. In contrast, the treated LLZO particles seem to integrate better into the matrix, as can be observed in Figure 2g, displaying a higher homogeneity of the surface. Incidental powder agglomerates are observed in both films, as shown in the cross-section SEM images in Figure S4.

The total ionic conductivity of the SPE and CPEs with the non-treated and boron-treated LLZO ceramic particles was investigated by electrochemical impedance spectroscopy (EIS) with the CPE/SPE sandwiched between two stainless steel blocking electrodes within the temperature range of 30–100 °C. The ionic conductivity behaviour of the CPEs was investigated for two different LLZO particle loadings: 20 and 40 wt%. From now on, the CPEs with treated LLZO particles are referred to as CPE20BT and CPE40BT, for the 20 and 40 wt% additions, respectively, while the CPEs with non-treated LLZO particles are analogously labelled as CPE20NT and CPE40NT.

As shown in Figure 3a, the highest bulk resistance is observed for the neat SPE, and the resistance which becomes

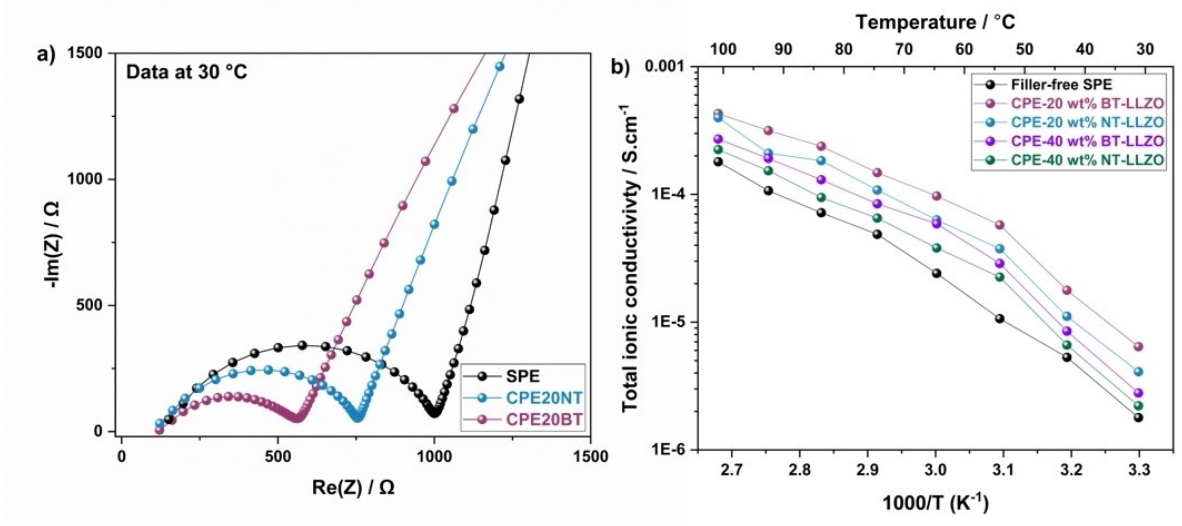

Figure 3. (a) Nyquist plot profiles of the SPE, CPE20NT, and CPE20BT films at 30 °C. (b) Arrhenius plots of the SPE and various CPEs with 20 and 40 wt% of NT (non-treated) and BT (boron-treated) LLZO particles within the temperature range of 30–100 °C.

reduced after incorporating LLZO particles for both CPE20BT and CPE20NT. This suggests that the addition of LLZO ceramic filler contributes to enhance the overall ionic conductivity of CPEs in different ways. Firstly, LLZO addition could promote the segmental motion of PEO. To confirm this, DSC measurements were carried out to compare the glass transition temperature (T_g) changes before and after incorporating LLZO particles. As shown in Figure 2b, when compared to the SPE as a reference, the T_g is reduced for both CPE20NT and CPE20BT, indicating a more flexible polymer matrix, possibly as a result of reduced polymer crystallinity.

The Nyquist plots of SPE, CPE20NT and CPE20BT in Figure 3a all display a semicircle at high and medium frequency ranges. For the SPE, this is normal and can be assigned to the migration of ions in the bulk of the polymer matrix.[49] Upon adding ceramic particles, it is clear that the resistance decrease and that the semicircle becomes more depressed for both CPE20NT and CPE20BT samples. The conductivity values are, however, not close to those reported for LLZO, and it is therefore plausible that the conductivity captured in the Nyquist plot is also associated with conductivity in primarily the polymer phase, but that it is aided by the interfaces introduced by the particles. The different shapes of the semi-circle also indicate a combination of transport paths, considering that an extra capacitance appears due to the introduction of interfaces in the bulk electrolyte.[50] There is, however, no conclusive evidence of the bulk phase of LLZO contributing to the bulk CPE ionic transport, which could then be translated into obtaining a significantly higher overall ionic conductivity. In fact, such superior bulk Li-ion conductivity of LLZO can only be achieved when the ceramic particles are pressed,and sintered at high temperatures in order to establish an intimate particle–particle contact for sustaining continuous Li-ion transport through an ion hopping mechanism. Presuming such LLZO bulk Li-ion conductivity contribution to the overall ionic conductivity of the CPEs, one should obtain higher conductivities at higher ceramic loadings. However, previously reported results have shown that increasing the ceramic content can rather have a detrimental effect on the conductivity of CPEs and no indication of bulk LLZO conduction is seen in such materials.[14,33]

The Arrhenius plots in Figure 3b show clearly that the CPEs with boron-treated LLZO particles display improved ionic conductivities compared to the filler-free SPE and the CPEs with non-treated LLZO particles. The highest ionic conductivity is reached at 20 wt% of LLZO loading, which was therefore chosen for further electrochemical characterization. CPEs with 40 wt% of either NT or BT LLZO particles still display a higher ionic conductivity compared to that of the neat SPE, yet lower than that of the CPEs with 20 wt% of the ceramic filler. This may suggest that higher ceramic loadings could have a detrimental effect on the ionic conduction in the CPEs due to the formation of agglomerates that can hinder or block the ionic transport pathways in the composite system.[21] The most interesting observation is, however, that the CPE20BT and CPE40BT samples exhibit a higher ionic conductivity compared to that of the CPE20NT and CPE40NT, respectively. This shows that the surface treatment has an effect on the ionic conductivity, possibly through additional ion conduction pathways along the polymer–ceramic interfaces that are more accessible in the boron-treated LLZO particle system. This is in good agreement with the hypothesis that the detrimental Li_2CO_3 layer on the surface of the LLZO particles severely hinders ionic transport, and that its removal through a H_3BO_3 surface treatment is thereby beneficial for the overall ionic conduction in CPEs.

To further explore the potential of BT-LLZO, the cationic transference number T_+ was investigated for the filler-free PEO-based SPE and the CPEs with 20 wt% of NT and BT LLZO. T_+ is a key factor for limiting Li filament formation/growth in solid-state batteries: the higher the T_+, the less likelihood for Li

filament formation.[51] T_+ was estimated by means of the Bruce–Vincent method, i.e., by combining a potentiostatic polarization measurement with measuring the impedance of a Li symmetrical cell at the initial state and after being polarized when the current has reached a steady-state;[52,53] see Figure 4a for CPE20BT and Figure S7 for SPE and CPE20NT, respectively. After fitting the impedance data using the equivalent circuit shown in Figure S8, the initial and steady-state bulk and interfacial resistances could be determined, from which the T_+ was calculated by using Equation (1) in the Experimental section. As it can be seen in Figure 4b, it is clear that the transference number increases after incorporating the LLZO particles into the SPE, similarly to the trend earlier observed for the ionic conductivity. It is thus seen that the T_+ for CPE20BT is higher than that of CPE20NT. The differences between the treated and non-treated LLZO particles are correlated to the ζ-potential data discussed above, which indicates a possible favourable interaction with the LLZO surface after the surface treatment. Such interactions are less likely for pristine LLZO particles that are covered by an unwanted layer of lithium carbonate on their surface. Still, the cation transference numbers are notably low and well in the range of the PEO:LiTFSI SPE itself, again suggesting that bulk conduction through the LLZO particles (which are expected to have $T_+ = 1$) is not a major mode of ion transport in any of the CPE systems.

Considering the enhanced conductivity and T_+ for CPE20BT, the rate capability and cycling performances of this particular composite electrolyte were explored and compared to those of CPE20NT. CPEs with a thickness around ~70 μm were sandwiched between an LFP electrode and a Li metal anode in a pouch cell configuration. Galvanostatic cycling was carried out firstly at a C-rate of 0.05 C at 60 °C between 2.7 and 4.2 V; see Figure 5&6a. CPE20BT delivered a low initial discharge capacity of 124.7 mAh g^{-1}, which can be explained by the formation of an initial SEI, after which the capacity stabilized in subsequent cycles and maintained a constant value around 156 mAh g^{-1}, indicating no further build-up of decomposition products on the anode side. Compared to CPE20NT, the difference in the discharge capacity between the first and the next cycles is not that striking. However, a clear difference between the charge and discharge capacity was observed, corresponding to a higher coulombic efficiency for CPE20BT as compared to CPE20NT, i.e. ~99.22 % *vs.* ~96.37 %, and fluctuating during cycling as displayed in Figure 5. This indicates that the facile LLZO surface treatment also supports a stable cathode/electrolyte interface and therefore the occurrence of any side reactions is largely circumvented.[28,54,55]

The rate capability of CPE20BT was also investigated between 0.05 and 1 C; see Figure 6a. The cell exhibits a rather high cycling stability with discharge capacities not lower than 110 mAh g^{-1} up to 1 C rate, recovering its initial capacity when returning to 0.05 C, and maintaining a stable coulombic efficiency (~99 %) throughout 200 cycles. It is also worth noting that the CPE20BT exhibits better rate performance compared to its CPE20NT counterpart, which instead shows an erratic behaviour for the corresponding cell voltage when cycled at 1 C, as seen in Figure S9. CPE20NT also exhibits a more pronounced capacity decay: from 159 mAh g^{-1} at 0.05 C to 116 mAh g^{-1} at 0.1 C, resulting in a capacity loss of 27 %. This could possibly be explained by limitations due to poor polymer-ceramic interfacial transport, as previously reported for LLZO-based CPEs.[48]

As mentioned above, the surface treatment of LLZO could also enable a better adhesion of the ceramic particles with the polymer matrix, lower interfacial resistance, and thereby Li filament suppression after Li_2CO_3 removal.[56] To demonstrate the capability of the treated electrolyte material, the cycling stability of CPE20BT *vs.* Li metal was tested in symmetrical cells at 60 °C by applying a series of increasing current densities from 0.1 to 1 mAh cm^{-2}; the results are shown in Figure 6b. The resulting voltage profile of the Li//CPE20BT//Li cell cycled at the lowest current density (0.1 mAh cm^{-2}) is stable with a slight polarization voltage observed for the first 10–20 cycles (Figure S11a), indicating the formation of a stable SEI between the

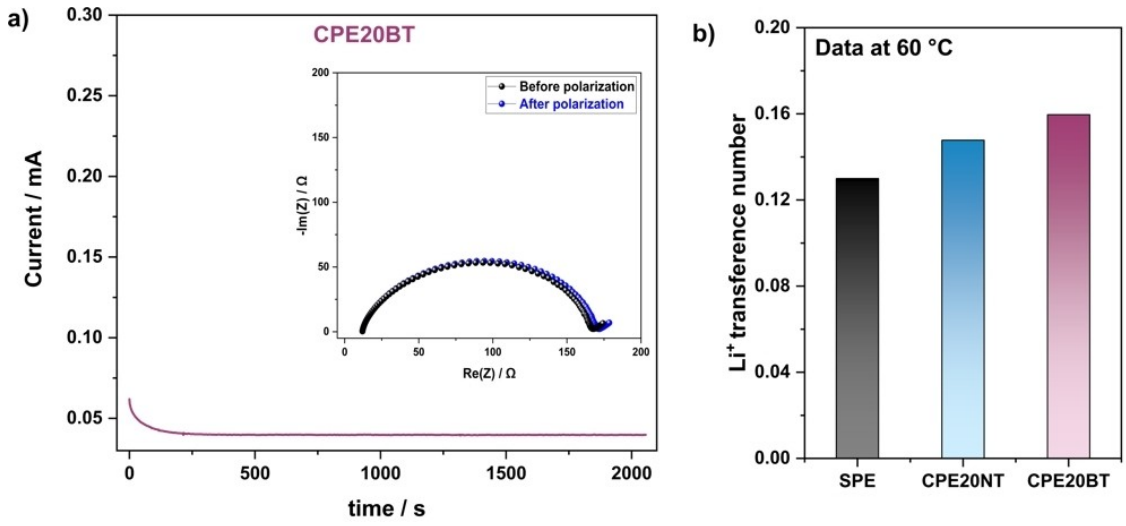

Figure 4. (a) Chronoamperometric response of Li//CPE20BT//Li symmetrical cells at 60 °C. Inset: Nyquist plots before and after polarization. (b) Li^+ transference number of the SPE, CPE20NT and CPE20BT samples at 60 °C.

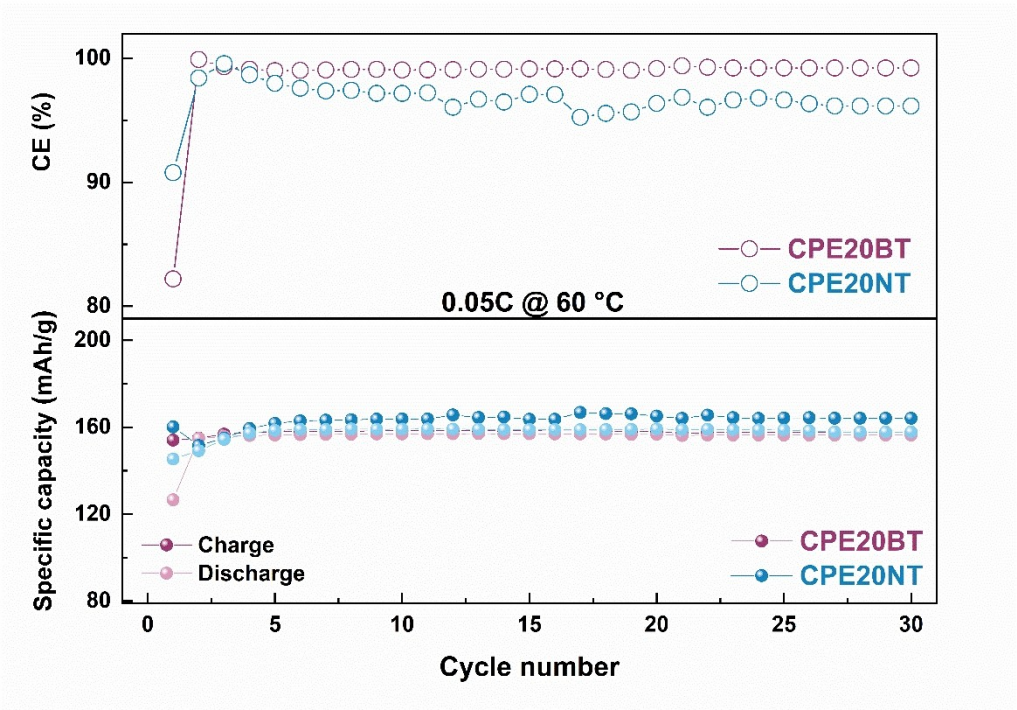

Figure 5. Cycling performances/Coulombic efficiency *vs.* cycle number of CPEs with 20 wt% of NT and BT LLZO particles at 60 °C.

CPE and the Li metal.[57] Upon increasing the current density, the cell cycling remained stable and only a minuscule overpotential of 15.8 mV was detected upon transitioning from 0.1 to 0.5 mA cm^{-2}, and 25.0 mV when switching from 0.5 to 1.0 mA cm^{-2}, as seen in Figure S11. CPE20BT demonstrates long-term cycling stability over 700 h at current densities as high as 1 mA cm^{-2}, indicating excellent interfacial stability against Li metal, thereby enabling good electrochemical performance of CPE20BT in Li-metal batteries. Finally, a comparison of the cycling performances of CPE20BT and CPE20NT in Li-LFP cells subjected to the same rate capability test (Figure S12) confirmed superior cycling features for the cell with CPE20BT, thus further corroborating the validity of this approach with B-based surface-modification of LLZO particles for aimed uses in CPEs.

Conclusions

Solid composite electrolytes constitute complex systems in which the interaction between the polymer matrix and ceramic particles can often play a more important role than the phases themselves. In this work, one fundamental issue has been addressed when using one of the most promising active ceramic fillers: LLZO. The spontaneous formation of a Li_2CO_3 layer on the surface of LLZO represents the main shortcoming limiting the ionic transport and electrochemical properties of LLZO-based CPEs. Here, we show that a facile acid surface treatment of LLZO particles can enable the removal of Li_2CO_3 from the LLZO surface without inducing any structural changes. CPEs with treated and non-treated LLZO particles were fabricated and their ionic conduction and electrochemical properties were compared. The Li_2CO_3-free LLZO:CPE shows an improved ionic conductivity and higher Li^+ transference number compared to the Li_2CO_3-containing LLZO:CPE. We hypothesize that this is due to an enhanced ionic transport at the polymer–ceramic interface. These enhanced ionic transport properties resulted in better electrochemical performance of the boron-treated LLZO:CPE in terms of a higher coulombic efficiency (~99%) and better cycling capability at higher C-rates compared to the non-treated LLZO:CPE. In addition, the boron surface treatment of LLZO contributes to a significantly better cycling stability *vs.* Li metal at higher current densities (1 mA cm^{-2}) over 700 hours. This study highlights the importance of surface chemistry engineering of ceramic particles for a better design of CPEs for solid-state Li-metal batteries.

Experimental Procedure

Materials Synthesis

LLZO

$Li_{6.4}La_3Zr_{1.4}Ta_{0.6}O_{12}$ was synthesized via a solid-state synthesis using Li_2CO_3 (Sigma-Aldrich, 99.99% trace metal basis), $La(OH)_3$ (Sigma-Aldrich, 99.99% trace metal basis), ZrO_2 (Sigma-Aldrich, 99% trace metal basis) and Ta_2O_5 (Sigma-Aldrich, 99% trace metal basis) as initial precursors. The precursors were mixed in a weighing boat prior to introduction into a Retsch Planetary Ball Mill PM200. From the given stoichiometry, a 20% excess of lithium carbonate precursor was purposely introduced in order

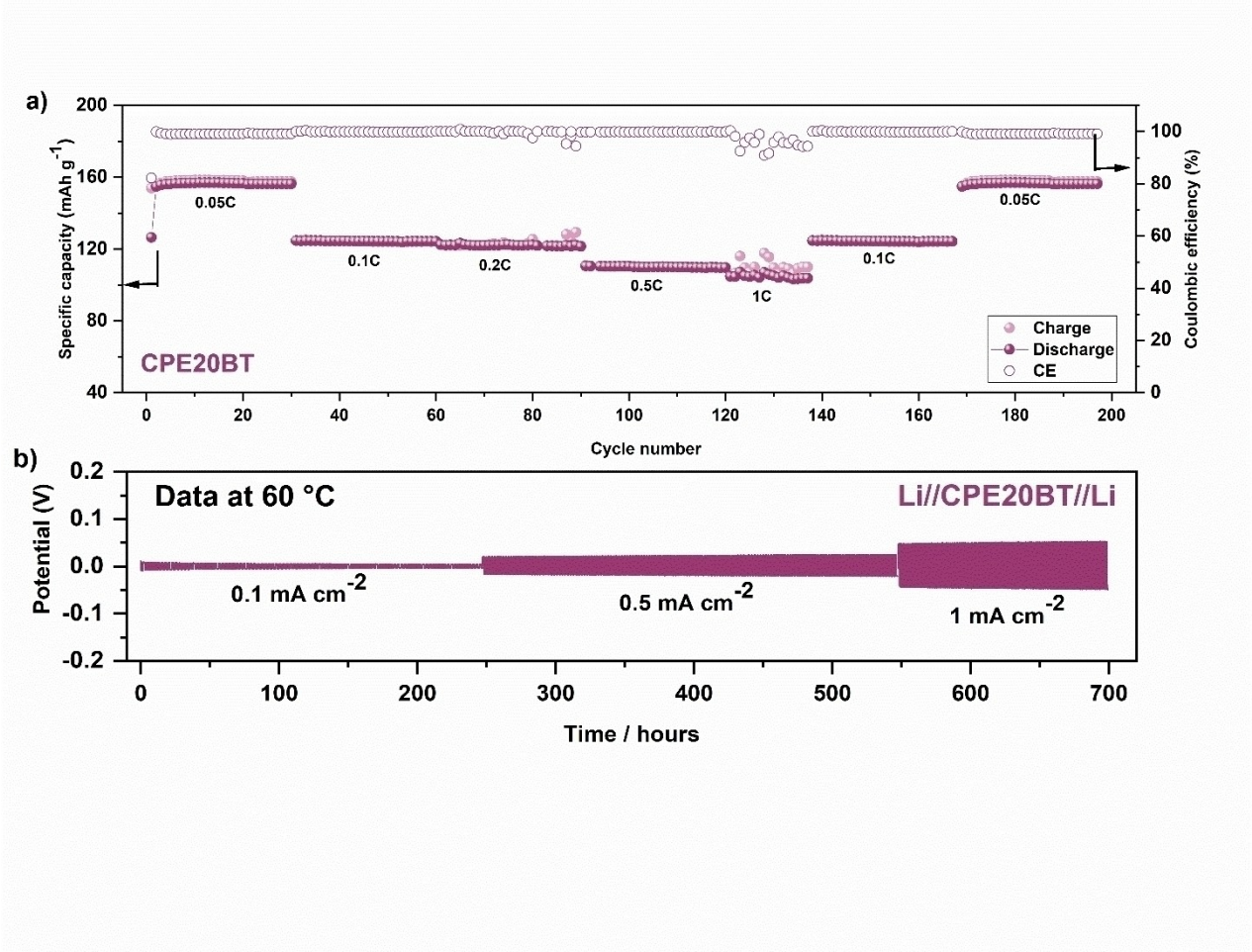

Figure 6. (a). Rate performances from C/20 up to 1 C and coulombic efficiency of LFP//CPE20BT//Li battery cells at 60 °C. (b). Long-term cycling of Li//CPE20BT//Li symmetrical cells with increasing plating/stripping current density at 60 °C.

to compensate for the volatilisation of lithium during the subsequent high-temperature synthesis steps. Elemental substitution of zirconium by tantalum was carried out to ensure both the stabilisation of the highly conductive cubic phase and the enhancement of the Li-ion conductivity values of the ceramic bulk.[58–61] The mix of precursors was wet-milled in 2-propanol using yttria-stabilised zirconia jars for 12 h at 450 RPM. The resulting mixture was dried and then placed in alumina crucibles for high-temperature phase formation. The powders were placed in a Carbolite Gero High Temperature Bottom Loading furnace and maintained at a temperature of 950 °C for 20 hours, ramping to and from that temperature at a rate of 2 °C/min. An intermediate step of 4 h at 700 °C while heating was introduced to promote carbon volatilisation.[21,29] Additional milling of the synthesised LLZO powders was performed on the same planetary ball mill for 6 h at 450 RPM in order to reduce the grain size and homogenise the resulting powders. Powders were then dried and quickly introduced into an argon-filled glovebox, where they were sieved by using a 63 μm mesh size sieve to further control the maximum dimensions of the powders.

Inside the glovebox, equal masses of LLZO powders were kept separated in order to compare those with surface modification versus unmodified ("pristine") ones. The pristine powders were continuously kept inside the argon-filled glovebox until further characterisation. The to-be modified powders were removed from the glovebox and placed in a closed vial filled with a boric acid (Sigma-Aldrich ACS reagent 99.5 %) solution in ethanol (5 g/100 mL) under vigorous stirring for 24 h. Afterwards, the suspension with the modified LLZO particles was placed in centrifuge vials to separate the acid solution from the solid by using an Eppendorf Centrifuge 5430 operated at 7000 RPM for 3 min. The sedimented particles were then briefly dried in a ventilated oven, prior to subsequent introduction into the glovebox, where they were finally sieved.

SPE & CPE Film Preparation

Solid polymer electrolyte (SPE) and composite polymer electrolyte (CPEs) films were fabricated through a controlled solvent evaporation solution casting method as described previously.[17] Firstly, a solution of poly(ethylene oxide) (PEO) ($M_w = 2\ 000$

000 g/mol; Sigma-Aldrich) combined with 30 wt% LiTFSI in acetonitrile was prepared, to which 20 and 40 wt% (relative to the SPE) of LLZO ceramic particles (both non-treated and boron-treated) was added. For SPE films, the PEO–LiTFSI solution was directly transferred to dedicated PTFE moulds. For CPEs, the polymer–salt–LLZO–solvent mixture was ball-milled at 25 Hz for 15 min, and then transferred to Teflon molds. After vacuum drying for 60 h at 60 °C, self-standing films of 16 mm in diameter were punched out and their thickness ranged approximately between 50 and 100 μm.

Cell Assembly

Positive electrodes were prepared by mixing 75 wt% of active material (LFP, Phosphotech), 10 wt% carbon black (C65, Imerys), and 15 wt% of PEO as binder in acetonitrile. The mixture was ball-milled at 30 Hz for 30 min and the obtained slurry was coated using a 150 μm doctor blade on a carbon-coated Al foil with a 150 μm film applicator (ZFR 2040 4-sided Applicator, Zehntner GmbH Testing Instruments). The slurry coating was dried in a vacuum oven at 80 °C for 12 h before cutting electrodes of 13 mm in diameter. The electrodes were thereafter dried under vacuum in a Büchi oven at 120 °C for 12 h inside an Ar-filled glovebox before cell assembly. Electrochemical characterization was performed using a pouch cell configuration with lithium foil as simultaneous negative electrode and reference.

Physico-Chemical Characterisation

Both powders and films were subjected to several characterisations to uncover the differences between the modified and unmodified LLZO particles and their respective CPE films. X-Ray diffraction (XRD) was carried out via a Bruker D8 Advance diffractometer in Bragg-Brentano configuration, using a Cu–Kα source (1.5406 Å). LLZO powder samples were backloaded in silicon sample holders, while the electrolyte films were placed on top of a flat special silicon wafer holder. All diffractograms were acquired at room temperature (≈21 °C) and regular atmosphere in the 2θ angular range of 10–80°, using increments of 0.01° and 1 s per step. Peak assignment was performed by using both the Diffrac.Eva software and the Inorganic Crystal Structure Database.[63]

Thermal properties of SPE and CPEs were evaluated by differential scanning calorimetry (DSC) on a Mettler Toledo DSC 3+ instrument. Samples were hermetically sealed in Al pans, and the heat flow was measured between 150 and −50 °C in a heat–cool–heat cycle at a heating rate of 10 °C/min and cooling rate of 5 °C/min. The glass transition temperature, T_g, was determined from the midpoint of change in heat capacity.

X-Ray Photoelectron Spectroscopy (XPS) was performed on both powders and films using a Kratos Axis Supra+ spectrometer. Spectra were acquired by using a monochromatic Al Kα radiation (1486.6 eV), an emission current of 15 mA and a pass energy of 20 eV. As all tested materials are electronically non-conductive, a charge neutraliser was used while measuring. The resulting spectra were fitted via the CasaXPS software, using the GL(30) lineshape for the simulated peaks, a Shirley-type background and using C–C/C–H carbon peak at 284.8 eV as calibration reference.

LLZO powders, CPEs morphology and ceramic particle distribution in the polymer matrix were evaluated by scanning electron microscopy (SEM) on a Zeiss/LEO 1530 SEM equipment. Top and cross-section images were acquired at a ~6.3 mm working distance, with an applied acceleration voltage of 1 kV, a 100 pA probing current and an in-lens detector. Samples were placed onto the SEM stubs under argon and transferred to the SEM with no further modification.

Fourier-Transform infrared spectroscopy (FTIR) measurements were carried out using a Perkin–Elmer Spectrum One FT-IR spectrometer equipped with a ZnSe crystal attenuated total reflectance (ATR) setup at room temperature. FT-IR spectra were recorded from 4000 to 650 cm^{-1} with a 4 cm^{-1} resolution measuring 32 scans on the as-synthesized CPE films.

Dynamic Light Scattering (DLS) and Zeta (ζ) potential measurements were performed in a Malvern Zetasizer Nano ZS equipment using PMMA disposable cuvettes and disposable folded capillary Zeta Cells, respectively. The ceramic LLZO powders were suspended in isopropanol at an initial concentration of 0.022 g/mL, and such suspension was further diluted 1:5 in isopropanol to ensure proper quality of the retrieved data, according to the quality indicators directly provided by the equipment thorough its software. The final dilutions were sonicated immediately before the DLS and ζ-potential measurements to favour the dispersion of the powders and break up the particle agglomerates. The employed refractive index and absorption rate for the two LLZO samples were, respectively, 1.4 and 0.1.[64]

Electrochemical Characterisation

Ionic Conductivity

The total ionic conductivity was measured by a Schlumberger SI 1260 impedance/Gain-phase analyzer for the SPE and CPE films sandwiched between two stainless-steel electrodes in a CR2025 coin cell configuration. The measurements were carried out from 7 MHz to 100 mHz with an AC sinusoidal amplitude of 10 mV while progressively increasing the temperature up to 90 °C with steps consisting of 10 °C intervals. The assembled cells were heated at 90 °C for 1 h one day before the measurements to improve the interfacial contact.

Transference Number

Li^+ transference numbers were determined electrochemically using the Bruce–Vincent method which was performed on a Bio-Logic SP-240 potentiostat at 60 °C. Symmetrical pouch cells were assembled using a SPE/CPE film of 16 mm in diameter sandwiched between two 12 mm- diameter lithium disks. The

cells were kept at 60 °C overnight prior to the measurements. The lithium transference number, T_+ was determined from the equation below:[52]

$$T_+ = \frac{I_{SS}(\Delta V - I_0 R_0)}{I_0(\Delta V - I_{SS} R_{SS})} \quad (1)$$

where $\triangle V$ is the applied polarization voltage, I_0 and R_0 are the initial current and resistance, respectively, and I_{SS} and R_{SS} are the steady-state current and resistance, respectively. The measurements were carried out between 7 MHz and 100 mHz with an amplitude of 10 mV and a bias of 0 and 10 mV before and after polarization, respectively.

Li Stripping/Plating

To assess the cycling stability of the CPEs *vs.* Li metal, Li stripping/plating experiments were carried out at 60 °C in two-hour cycles while increasing the current density from 0.1 up to 1 mA cm^{-2} on a Bio-Logic MPG instrument. Symmetrical pouch cells were assembled with lithium metal discs of 12 mm diameter and the composite electrolyte of 16 mm in diameter. The cells were left resting at 60 °C overnight prior to measurements.

Galvanostatic Cycling

Cell cycling was carried out at 60 °C by applying a C-rate of C/20 based on a theoretical capacity of 163 mAh g^{-1} (areal capacity of ~1.3 mAh cm^{-2}) within a voltage window of 2.7–4.2 V on an ARBIN BT-2043 cycling station to perform galvanostatic charge-discharge tests. Pouch cells enclosing the CPE sandwiched between a 13 mm-diameter LFP cathode and a 15 mm-diameter Li metal anode were connected to the cycler and subsequently tested. Rate capability tests were also carried out following the same protocol as above while increasing the C-rate from C/20 to 1 C.

Author Contributions

Ignacio Cuevas[i]: Conceptualization, Methodology, Investigation, Writing-Original draft. **Kenza Elbouazzaoui**[i]: Conceptualization, Methodology, Investigation, Writing-Original draft. **Mario Valvo**: Writing-review & editing, Supervision, Funding acquisition. **Jonas Mindemark**: Writing-review & editing, Supervision, Funding acquisition. **Daniel Brandell**: Writing-review & editing, Supervision, Funding acquisition. **Kristina Edström**: Writing-review & editing, Supervision, Funding acquisition. [i] I. Cuevas & K. Elbouazzaoui contributed equally to this work.

Acknowledgments

This work was supported by STandUP for Energy, the Swedish Foundation for Strategic Research (project SOLID ALiBI, grant no. ST19-0095), the Swedish Excellence Center BASE funded by Vinnova and the European Research Council (ERC) under the European Horizon 2020 research and innovation programme (Grant agreement No. 771777 FUN POLYSTORE). M.V. acknowledges also the funding by the Swedish Electromobility Centre via the project no. 12038. Alina Oltean, Fredrik Lindgren and Pedro Berastegui are acknowledged for technical assistance in the labs. Tomas Edvinsson and Jakob Tyr are acknowledged for providing access to the DLS measurements.

Conflict of Interests

The authors declare no competing financial interests.

Data Availability Statement

The data that support the findings of this study are available from the corresponding author upon reasonable request.

Keywords: Composite polymer electrolytes · Surface treatment · LLZO · Ionic transport · Solid Li-metal batteries

[1] M. Armand, P. Axmann, D. Bresser, M. Copley, K. Edström, C. Ekberg, D. Guyomard, B. Lestriez, P. Novák, M. Petranikova, W. Porcher, S. Trabesinger, M. Wohlfahrt-Mehrens, H. Zhang, *J. Power Sources* **2020**, *479*, DOI: 10.1016/j.jpowsour.2020.228708.
[2] L. Bravo Diaz, X. He, Z. Hu, F. Restuccia, M. Marinescu, J. V. Barreras, Y. Patel, G. Offer, G. Rein, *J. Electrochem. Soc.* **2020**, *167*, 090559.
[3] F. H. Gandoman, J. Jaguemont, S. Goutam, R. Gopalakrishnan, Y. Firouz, T. Kalogiannis, N. Omar, J. Van Mierlo, *Appl. Energy* **2019**, *251*, 113343.
[4] J. Duan, X. Tang, H. Dai, Y. Yang, W. Wu, X. Wei, Y. Huang, *Electrochem. Energ. Rev* **2020**, *3*, 1– 42.
[5] R. Gond, W. Van Ekeren, R. Mogensen, A. J. Naylor, R. Younesi, *Mater. Horizons* **2021**, *8*, 2913–2928.
[6] N. Boaretto, I. Garbayo, S. Valiyaveettil-SobhanRaj, A. Quintela, C. Li, M. Casas-Cabanas, F. Aguesse, *J. Power Sources* **2021**, *502*, DOI: 10.1016/j.jpowsour.2021.229919.
[7] R. I. Pushparaj, A. R. Kumar, G. Xu, *J. Energy Storage* **2023**, *72*, 108493.
[8] J. Janek, W. G. Zeier, *Nat. Energy* **2023**, *8*, 230–240.
[9] J. Janek, W. G. Zeier, *Nat. Energy* **2016**, *1*, DOI: 10.1038/nenergy.2016.141.
[10] D. Zhang, X. Xu, Y. Qin, S. Ji, Y. Huo, Z. Wang, Z. Liu, J. Shen, J. Liu, *Chem. - A Eur. J.* **2020**, *26*, 1720–1736.
[11] Y. Su, F. Xu, X. Zhang, Y. Qiu, H. Wang, *Nano-Micro Lett.* **2023**, *15*, 82.
[12] G. Polizos, M. Goswami, J. K. Keum, L. He, C. J. Jafta, J. Sharma, Y. Wang, L. T. Kearney, R. Tao, J. Li, *ACS Nano* **2024**, *18*, 2750–2762.
[13] H. Huo, Y. Chen, J. Luo, X. Yang, X. Guo, X. Sun, *Adv. Energy Mater.* **2019**, *12*, 1–8.
[14] J. Mindemark, M. J. Lacey, T. Bowden, D. Brandell, *Prog. Polym. Sci.* **2018**, *81*, 114–143.
[15] D. Zhou, D. Shanmukaraj, A. Tkacheva, M. Armand, G. Wang, *Chem* **2019**, *5*, 2326–2352.
[16] N. Boaretto, L. Meabe, M. Martinez-Ibañez, M. Armand, H. Zhang, *J. Electrochem. Soc.* **2020**, *167*, 070524.
[17] K. Elbouazzaoui, F. Nkosi, D. Brandell, J. Mindemark, K. Edström, *Electrochim. Acta* **2023**, *462*, 142785.
[18] L. Chen, Y. Li, S. P. Li, L. Z. Fan, C. W. Nan, J. B. Goodenough, *Nano Energy* **2018**, *46*, 176–184.

[19] T. Yang, J. Zheng, Q. Cheng, Y. Y. Hu, C. K. Chan, *ACS Appl. Mater. Interfaces* **2017**, *9*, 21773–21780.
[20] J. Zheng, Y. Y. Hu, *ACS Appl. Mater. Interfaces* **2018**, *10*, 4113–4120.
[21] Z. Li, H. M. Huang, J. K. Zhu, J. F. Wu, H. Yang, L. Wei, X. Guo, *ACS Appl. Mater. Interfaces* **2019**, *11*, 784–791.
[22] J. Zheng, M. Tang, Y. Hu, *Angew. Chemie* **2016**, *128*, 12726–12730.
[23] J. Zagórski, B. Silván, D. Saurel, F. Aguesse, A. Llordés, *ACS Appl. Energy Mater.* **2020**, *3*, 8344–8355.
[24] P. Ghorbanzade, A. Pesce, K. Gómez, G. Accardo, S. Devaraj, P. López-Aranguren, J. M. López del Amo, *J. Mater. Chem. A* **2023**, *11*, 11675–11683.
[25] A. Gupta, J. Sakamoto, *Electrochem. Soc. Interface* **2019**, *28*, 63–69.
[26] K. Nie, S. Wu, J. Wang, X. Sun, Z. Yan, J. Qiu, Q. Yang, R. Xiao, X. Yu, H. Li, L. Chen, X. Huang, *ACS Appl. Mater. Interfaces* **2021**, *13*, 38384–38393.
[27] A. Sharafi, S. Yu, M. Naguib, M. Lee, C. Ma, H. M. Meyer, J. Nanda, M. Chi, D. J. Siegel, J. Sakamoto, *J. Mater. Chem. A* **2017**, *5*, 13475–13487.
[28] A. Sharafi, E. Kazyak, A. L. Davis, S. Yu, T. Thompson, D. J. Siegel, N. P. Dasgupta, J. Sakamoto, *Chem. Mater.* **2017**, *29*, 7961–7968.
[29] I. Cuevas, F. Nkosi, K. Edström, M. Valvo, *Appl. Surf. Sci.* **2024**, *656*, 159611.
[30] S. Li, J. Wang, F. Ji, M. Wang, Z. Hu, S. Huo, S. Zhang, H. Cheng, Y. Zhang, *J. Power Sources* **2024**, *592*, 233969.
[31] H. Noh, D. Kim, W. Lee, B. Jang, J. S. Ha, J. H. Yu, *Energies* **2023**, *16*, 7695.
[32] P. Ranque, J. Zagórski, G. Accardo, A. Orue Mendizabal, J. M. López del Amo, N. Boaretto, M. Martinez-Ibañez, H. Arrou-Vignod, F. Aguesse, M. Armand, S. Devaraj, *Inorganics* **2022**, *10*, 81.
[33] Y. Ruan, Y. Lu, X. Huang, J. Su, C. Sun, J. Jin, Z. Wen, *J. Mater. Chem. A* **2019**, *7*, 14565–14574.
[34] S. Vema, F. N. Sayed, S. Nagendran, B. Karagoz, C. Sternemann, M. Paulus, G. Held, C. P. Grey, *ACS Energy Lett.* **2023**, *8*, 3476–3484.
[35] M. Cai, J. Jin, T. Xiu, Z. Song, M. E. Badding, Z. Wen, *Energy Storage Mater.* **2022**, *47*, 61–69.
[36] M. J. Lee, D. O. Shin, J. Y. Kim, J. Oh, S. H. Kang, J. Kim, K. M. Kim, Y. M. Lee, S. O. Kim, Y. G. Lee, *Energy Storage Mater.* **2021**, *37*, 306–314.
[37] N. Hamao, K. Kataoka, N. Kijima, J. Akimoto, *J. Ceram. Soc. Japan* **2016**, *124*, 678–683.
[38] Z. Li, J. Fu, X. Zhou, S. Gui, L. Wei, H. Yang, H. Li, X. Guo, *Adv. Sci.* **2023**, *10*, 1–18.
[39] X. Zhang, J. Xie, F. Shi, D. Lin, Y. Liu, W. Liu, A. Pei, Y. Gong, H. Wang, K. Liu, Y. Xiang, Y. Cui, *Nano Lett.* **2018**, *18*, 3829–3838.
[40] J. Zagórski, J. M. López Del Amo, M. J. Cordill, F. Aguesse, L. Buannic, A. Llordés, *ACS Appl. Energy Mater.* **2019**, *2*, 1734–1746.
[41] M. Kozdra, D. Brandell, C. M. Araujo, A. Mace, *Phys. Chem. Chem. Phys.* **2024**, *26*, 6216–6227.
[42] C. Zhang, S. Zhang, Y. Zhang, X. Wu, L. Lin, X. Hu, L. Wang, J. Lin, B. Sa, G. Wei, D. L. Peng, Q. Xie, *Small Struct.* **2024**, *5*, DOI: 10.1002/sstr.202300301.
[43] Y.-J. Lim, Y.-H. An, N.-J. Jo, *Nanoscale Res. Lett.* **2012**, *7*, 3–8.
[44] Z. Wang, X. Huang, L. Chen, *Electrochem. Solid-State Lett.* **2003**, *6*, 4–9.
[45] X. Gouin, P. Grange, L. Bois, P. L'Haridon, Y. Laurent, *J. Alloys Compd.* **1995**, *224*, 22–28.
[46] D. P. Button, L. S. Mason, H. L. Tuller, D. R. Uhlman, *Solid State Ionics* **1983**, *9–10*, 585–592.
[47] X. Zhang, J. Xiong, F. Chang, Z. Xu, Z. Wang, P. Hall, Y. J. Cheng, Y. Xia, *ACS Appl. Mater. Interfaces* **2022**, *14*, 45272–45288.
[48] H. Huo, X. Li, Y. Sun, X. Lin, K. Doyle-Davis, J. Liang, X. Gao, R. Li, H. Huang, X. Guo, X. Sun, *Nano Energy* **2020**, *73*, 104836.
[49] B. Sun, J. Mindemark, K. Edström, D. Brandell, *Solid State Ionics* **2014**, *262*, 738–742.
[50] H. K. Kim, P. Barai, K. Chavan, V. Srinivasan, *J. Solid State Electrochem.* **2022**, *26*, 2059–2075.
[51] L. Chen, W. Li, L. Z. Fan, C. W. Nan, Q. Zhang, *Adv. Funct. Mater.* **2019**, *29*, 1–11.
[52] J. Evans, C. A. Vincent, P. G. Bruce, *Polymer (Guildf).* **1987**, *28*, 2324–2328.
[53] P. G. Bruce, C. A. Vincent, *J. Electroanal. Chem.* **1987**, *225*, 1–17.
[54] Y. Li, B. Xu, H. Xu, H. Duan, X. Lü, S. Xin, W. Zhou, L. Xue, G. Fu, A. Manthiram, J. B. Goodenough, *Angew. Chemie - Int. Ed.* **2017**, *56*, 753–756.
[55] H. Huo, Y. Chen, N. Zhao, X. Lin, J. Luo, X. Yang, Y. Liu, X. Guo, X. Sun, *Nano Energy* **2019**, *61*, 119–125.
[56] H. Huo, Y. Chen, J. Luo, X. Yang, X. Guo, X. Sun, *Adv. Energy Mater.* **2019**, *9*, 1–8.
[57] Q. Pan, D. M. Smith, H. Qi, S. Wang, C. Y. Li, *Adv. Mater.* **2015**, *27*, 5995–6001.
[58] K. Ishiguro, H. Nemori, S. Sunahiro, Y. Nakata, R. Sudo, M. Matsui, Y. Takeda, O. Yamamoto, N. Imanishi, *J. Electrochem. Soc.* **2014**, *161*, A668–A674.
[59] Y. Zhu, J. G. Connell, S. Tepavcevic, P. Zapol, R. Garcia-Mendez, N. J. Taylor, J. Sakamoto, B. J. Ingram, L. A. Curtiss, J. W. Freeland, D. D. Fong, N. M. Markovic, *Adv. Energy Mater.* **2019**, *9*, 1–11.
[60] T. Thompson, J. Wolfenstine, J. L. Allen, M. Johannes, A. Huq, I. N. David, J. Sakamoto, *J. Mater. Chem. A* **2014**, *2*, 13431–13436.
[61] A. Logéat, T. Köhler, U. Eisele, B. Stiaszny, A. Harzer, M. Tovar, A. Senyshyn, H. Ehrenberg, B. Kozinsky, *Solid State Ionics* **2012**, *206*, 33–38.
[62] L. Cheng, M. Liu, A. Mehta, H. Xin, F. Lin, K. Persson, G. Chen, E. J. Crumlin, M. Doeff, M. Doe, *ACS Appl. Energy Mater.* **2018**, *1*, 7244–7252.
[63] D. Zagorac, H. Muller, S. Ruehl, J. Zagorac, S. Rehme, *J. Appl. Crystallogr.* **2019**, *52*, 918–925.
[64] Y. Ji, C. Zhou, F. Lin, B. Li, F. Yang, H. Zhu, J. Duan, Z. Chen, *Materials (Basel).* **2020**, *13*, DOI: 10.3390/ma13030560.

Manuscript received: June 20, 2024
Revised manuscript received: September 6, 2024
Accepted manuscript online: September 12, 2024
Version of record online: ■■, ■■